Design of an Imaging Motional Stark Effect Diagnostic for Edge Current Density Measurements on MAST-U

S. Gibson

February 13, 2019

1 Introduction

The Motional Stark Effect (MSE) diagnostic [1] is used routinely in fusion devices to infer the magnetic pitch angle. MSE measurements provide a strong constraint for plasma equilibrium reconstruction codes, which provide q profiles and the internal magnetic field structure. These parameters play an important role in determining plasma stability. This proposal outlines a design for an Imaging Motional Stark Effect (IMSE) diagnostic [2] which would be used for edge current density studies on MAST-U. The diagnostic setup is presented as well as its predicted performance in typical plasma scenarios. A budget is outlined for the cost of an initial prototype system and a time line over which the system could be implemented.

1.1 Principle of the Motional Stark Effect

High energy neutral deuterium or hydrogen atoms are injected into the plasma. Their motion through the magnetic field induces a strong Lorentz electric field $\mathbf{E} = \mathbf{V} \times \mathbf{B}$ in the rest frame of the beam atoms, as shown in Fig. 1. Collisions between the background plasma and neutral beam atoms gives rise to orthogonally polarized and Stark split light emission. The multiplet is Doppler shifted away from the main D_α line and so can be isolated using bandpass filters. An example of the full energy component of the MSE spectrum is given in Fig. 2. However the spectrum can be complicated due to contributions from the half and third energy beam components. When the emission is viewed perpendicular to the $\mathbf{E}$ field, the $\Delta m=0$ transition (π emission) is linearly polarized parallel to the electric field and the $\Delta m=\pm 1$ transition (σ emission) is linearly polarized perpendicular to the $\mathbf{E}$ field. The MSE diagnostic measures the orientation of this polarized emission, giving a local measurement of the magnetic pitch angle.

1.2 Conventional MSE on MAST-U

Conventional MSE systems typically use a pair of photo-elastic modulators (PEMs) and polariser, which encode the polarisation information as an intensity modulation for transmission through optical fibers. The light passes through a filterscope, which is a collection of lenses and a narrowband interference filter used to select either π or σ component of the multiplet. Light is then collected onto avalanche photodiodes (APDs). The current MSE system is shown for MAST in Fig.??, with 36 filterscope channels and a spatial resolution of 2.5cm [3]. The current system has a wide field of view, taking measurements from the magnetic axis out to the edge of the plasma (R=0.8m - R=1.45m). It provides good core constraint to equilibrium reconstruction, and so is beneficial for core MHD studies and q profile dynamics.

Edge current density measurements were previously made with the existing system [4]. However the analysis is heavily dependent on the way in which the equilibrium used to reconstruct the current profile is constrained. The current MSE system has 3-4 radial channels around the pedestal region. As the spatial resolution of the MSE system is coarse, this greatly increases the uncertainty in local measurements of the edge current density. However, an increase in the polarisation angle profile is observed between these channels at the plasma edge during H mode, which is thought to be indicative of the edge bootstrap current. With the capabilities of
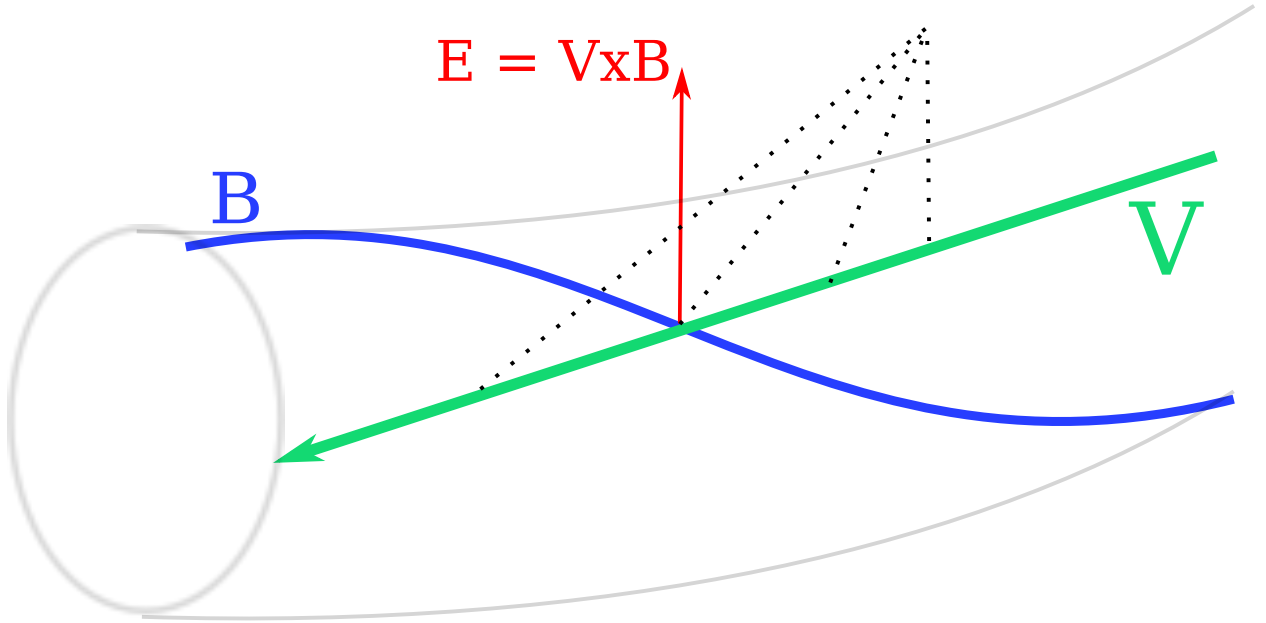
Figure 1: Neutral beam atoms travel at high velocity **v** (green) across a magnetic field (blue). This produces a Lorentz electric field (red) which causes Stark splitting of the energy levels in Hydrogen. Black dashed lines each represent a line of light along the neutral beam. Emission is red shifted as the neutral beam atoms move away from the observer.
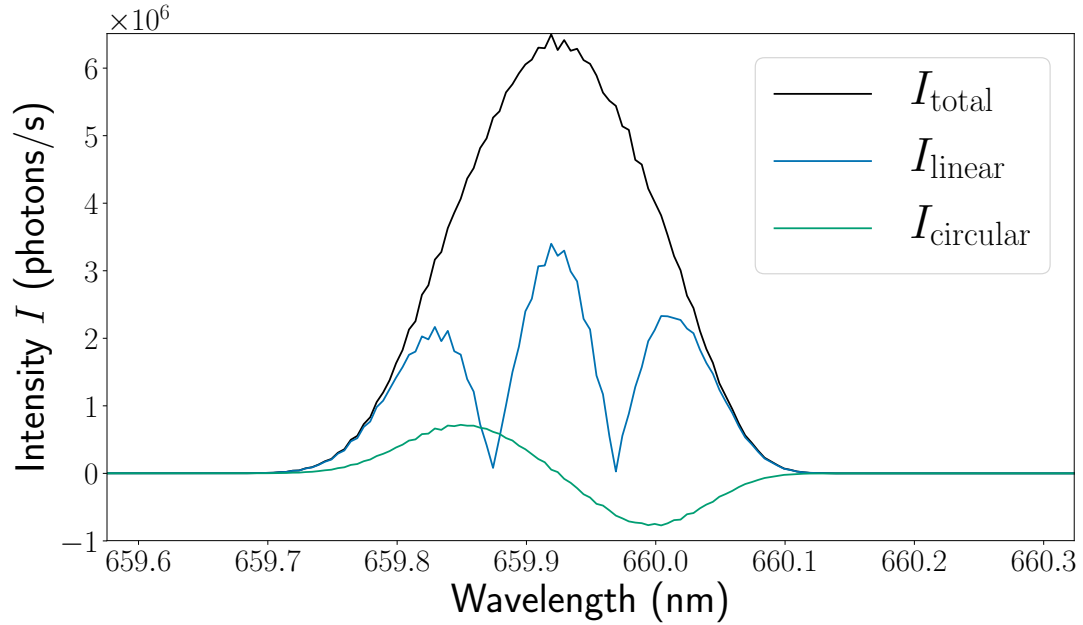

Figure 2: A modelled full energy component of the MSE spectrum (blue), showing the π wings and the central σ peak. As the toroidal B field is small on MAST-U, these π and σ peaks overlap, and a realistic MAST-U spectrum is shown in black. Some fraction of the emission is circularly polarised (green).

the existing diagnostic it would not be possible to thoroughly investigate edge current dynamics and make these current density measurements routine.
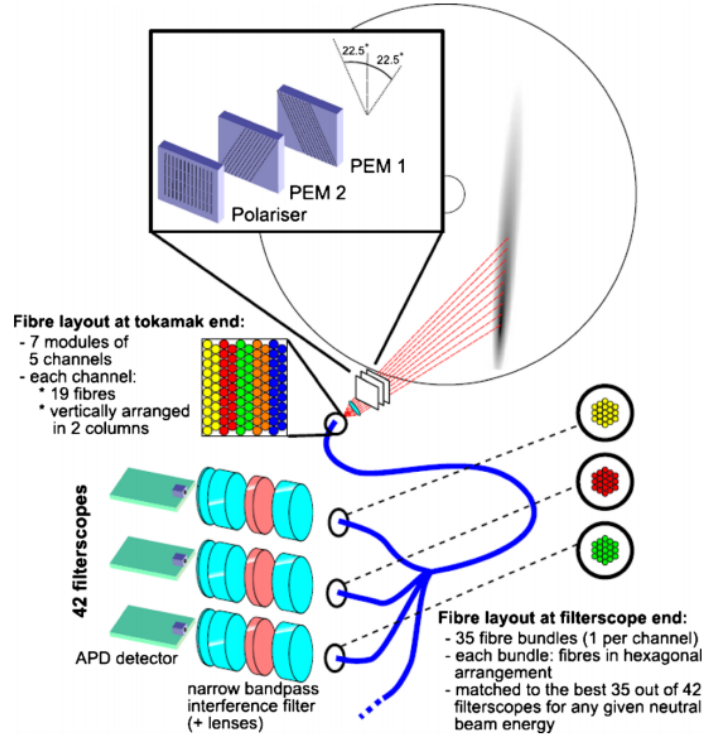

Figure 3: The current MAST-U conventional MSE system [3].

The size of the Stark splitting is dependent on magnetic field strength, beam velocity and line of sight (LOS) angle. A low toroidal field on MAST-U means the characteristic π and σ spectral features overlap, shown in Fig.2. Narrow-band interference filters with a full width half maximum (FWHM) = 0.1 nm are required for each radial channel to isolate either the π or σ polarized emission at a specific wavelength. Isolating a specific component of the multiplet omits a large fraction of the possible signal. Also, the Doppler shifted wavelength of the emission varies with neutral beam voltage and with the viewing angle between each LOS and the neutral beam. Fibre bundles need to be re-patched to alternative filterscopes to provide wavelength matching with the narrowband filters when the voltage varies by more than 1kV. The Doppler shift variation is also more prevalent on the inboard side where the angle between the line of sight and beam axis is small.

2 Imaging Motional Stark Effect

The imaging motional Stark effect (IMSE) diagnostic is a polarisation interferometer which captures 2D snapshot images of neutral beam emission [2]. Polarisation information is encoded as an interference pattern in the image, which is generated using birefringent waveplates. IMSE provides high spatial resolution, 2D measurement of the polarisation angle, which is particularly advantageous for constraining equilibrium reconstruction. The IMSE technique has been implemented on several other fusion devices such as ASDEX Upgrade for q profile changes during sawteeth crashes and fine variation in q at the magnetic axis [5].

2.1 Motivation for an edge IMSE system on MAST-U

Pedestal structures were investigated using an IMSE system on the K-STAR tokamak where the polarisation angle contours showed good agreement with equilibrium poloidal flux contours and enhanced radial structures

are visible [6]. The edge IMSE system proposed for MAST-U aims to provide local measurements of the edge current density for stability analysis. MAST-U has some strong advantages over conventional tokamaks specifically for edge current studies. MAST-U has a similar poloidal B field B_θ to that in conventional tokamaks, but lower B_ϕ, giving a wide range of polarisation angles and so changes in j_ϕ at the plasma edge should be much easier to detect [4]. In the tight aspect ratio limit $\epsilon = 1$ the bootstrap current is dominated by the poloidal field and pressure gradient rather than the density gradient,

$$j_{bs} = \frac{-1}{B_\theta}\frac{dp}{dr} \tag{1}$$

where p is the pressure and B_θ the poloidal magnetic field [7]. Combining high resolution Thompson scattering (HRTS) measurements of the pressure profile with local measurements of j_ϕ inferred from IMSE would provide a greater understanding of inter-ELM current dynamics, contributing towards improved stability analysis and independent verification of neoclassically derived current models.

At ASDEX-Upgrade (AUG) an IMSE system was developed for core physics studies. Combined with integrated data analysis techniques and equilbrium code CLISTE [8], they have seen significant improvements in the uncertainty of q min and across the q profile as a whole [9]. The designed IMSE system for MAST-U should still view some core plasma, and so could be implemented as a constraint to the equilibrium code EFIT++ if desirable.

2.2 Principle of IMSE

First considering polarised light emission of a given wavelength, one can represent this emission with a stokes vector S(λ),

$$S(\lambda) = \begin{bmatrix} S_0 \\ S_1 \\ S_2 \\ S_3 \end{bmatrix} = \begin{bmatrix} I_0(\lambda) \\ P_l(\lambda)\cos(2\gamma) \\ P_l(\lambda)\sin(2\gamma) \\ P_c(\lambda) \end{bmatrix} \tag{2}$$

where I_0 is the total light intensity, p_l is the fraction of the light which is linearly polarised and p_c the fraction of light which is circularly polarised and γ is the polariastion angle. Given that all only the first stokes component (ie. the light intensity) can be measured by CCDs, then the polarisation information needs to be encoded using either amplitude or phase modulation. The IMSE system is a spatial polarisation interferometer. Birefringent crystals impose a wavelength-dependent phase shift such that the orthogonal π and σ polarisation components constructively interfere. When combined with a polariser, this produces an interference pattern in the image plane. Using a ferro-electric crystal (FLC) waveplate, two successive images are taken, with the waveplate orientation at 45° and 90° which encodes the polarisation using phase modulation. The Mueller matrix of the optical system is given by,

$$\mathbf{M}_{\text{IMSE}} = R(\pi/4) \cdot W(\phi_{\text{QWP}}) \cdot R(-\pi/4) \cdot R(-\rho_{\text{FLC}}) \cdot W_{\text{FLC}} \cdot R(\rho_{\text{FLC}}) \cdot R(\pi/4) W(\phi_{\text{delay}}) \cdot R(-\pi/4) \cdot$$
$$R(\pi/4) \cdot W(\phi_{\text{displacer}}) \cdot R(-\pi/4) \cdot R(\pi/4) \cdot P \cdot R(-\pi/4) \tag{3}$$

where R is a rotation matrix around an orientation angle ρ, $W(\phi)$ is the Mueller matrix for a waveplate with retardance ϕ and P is the general Mueller matrix for a polariser with horizontal transmission. General Mueller matrices for each optical component can be found in Appendix A. The intensity transmitted by the IMSE system is then given by,

$$I(\lambda) = \frac{1}{2}S(\lambda) \cdot M_{\text{IMSE}} \tag{4}$$

where the transmitted intensity for each of the FLC states (ρ=45°, ρ=90°) is,

$$I_{45°}(\lambda) = \frac{1}{2}(S_0 + S_1\cos\phi(\lambda,y) + S_2\sin\phi(\lambda,y)) = \frac{I_0}{2}(1 + P_l\cos(\phi(\lambda,y) - 2\gamma)) \tag{5}$$

4

$$I_{90°}(\lambda) = \frac{1}{2}(S_0 + S_1 \cos\phi(\lambda, y) - S_2 \sin\phi(\lambda, y)) = \frac{I_0}{2}(1 + P_l \cos(\phi(\lambda, y) + 2\gamma)) \quad (6)$$

By taking an image in each FLC state, the sum of the phase demodulated images is the total phase shift imposed by the retarding components, and the difference is the polarisation angle 4γ.

2.3   Temporally Switched Single Spatial Heterodyne System

The IMSE system using the switching FLC, named the temporally switched single spatial heterodyne (TSSSH) system) is presented in Fig.4. The mathematical basis of the encoding technique was presented in Section 2.2. The optical system consists of:

- Collection lens f = 85mm NA = f/1.4

- Collimating lens f = 85mm

- Quarter waveplate

- Ferroelectric crystal switching waveplate of retardance 180°

- Delay plate of thickness L = 15mm and optical axis cut angle $\Theta = 0$ °

- Displacer plate of thickness L = 3mm, cut angle $\Theta = 45$ °

- A polariser oriented with axis at 45° to normal

- Filter with central wavelength λ_{CWL}=660nm, full width half maximum (FWHM) = 3nm

- Focussing lens f = 85mm NA = f/1.4

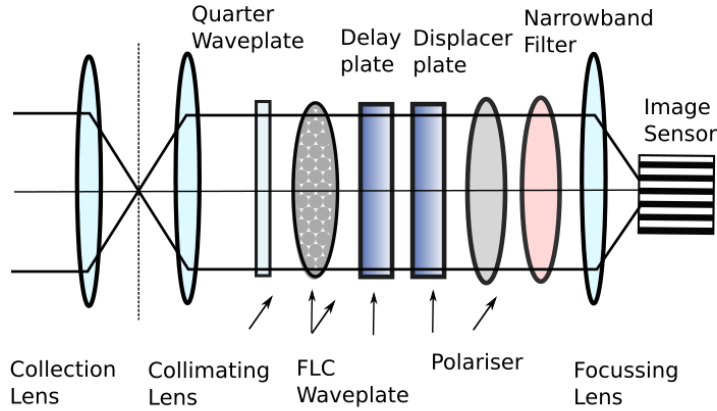- Detector in the imaging plane.

Figure 4: Optical setup of the switching IMSE system. The orientation axis is shown by the small arrow below each optical component. The interference pattern is shown on the detector.

2.4 Alternative Encoding Techniques

An alternative design of IMSE system is used at ASDEX, the amplitude spatial heterodyne (ASH) system. The ASH system replaces the FLC switching waveplate with a Savart plate, which consists of two birefringent waveplates with axes oriented 90° apart, both with optical axis cut angles of 45°. As light travels through the Savart plate, the ordinary and extraordinary components are switched as they enter the second plate. The savart plate creates zero net phase delay, but introduces a second orthogonal carrier frequency which produces sum and difference frequencies in the Fourier domain. This allows the polarisation angle to be captured in a single image. The amplitude system setup is shown in Fig.5. For the designed ASH system, a savart plate of thickness L=4.2mm is required.
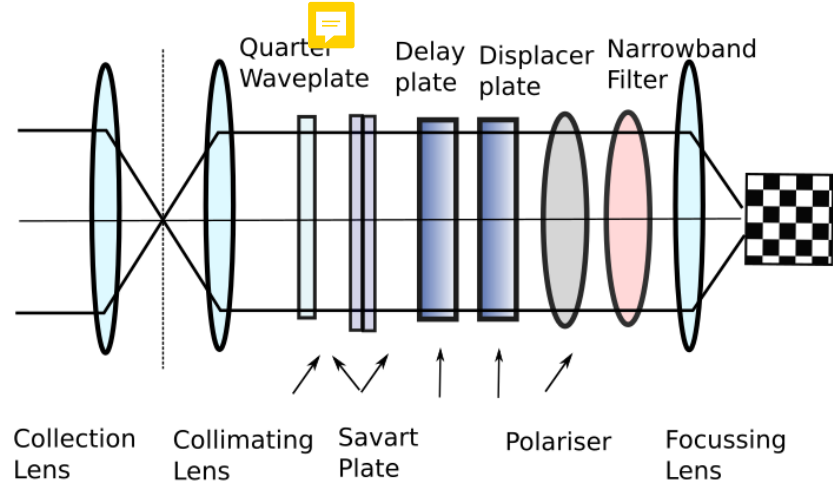

Figure 5: Optical setup of the amplitude spatial heterodyne (ASH) system. The orientation axis is shown by the small arrow below each optical component. If input light to the ASH system is completely linear, a checkerboard interference pattern is produced in the image plane.

An outline of the advantages and drawbacks of each technique are shown in Table.?? It would be beneficial to acquire both necessary components for the TSSSH and the ASH system in case of any severe retardance irregularities in the FLC waveplate.

All information encoded in single image	Improved radial resolution as fringe pattern can be orientated to maximize resolution for measuring sharp features
Reduced spatial resolution due to filtering around multiple carrier frequencies	Sensitive to fluctuations in beam voltage on the order of the camera exposure time
Requires some in situ calibrations	Requires camera triggering system linked to variation in beam voltage
Sensitive to circularly polarised light which can distort measurement	FLCs can have (temperature and stress dependent) non uniform retardance which distorts measurements

3 IMSE Capabilities

3.1 Spectrum Calculation

The MSE spectrum and emission intensity was forward modelled using the MSE modelling code MSESIM [10]. MSESIM takes into consideration collection volume effects, solid angle effects and variation in beam velocity distribution to give a realistic spectrum for each line of sight, as a function of wavelength. A plasma equilibrium was used from shot 18501, t=0.29s to provide a flux map and magnetic field. A neutral beam energy of 63keV was specified and the beam attenuation modelled using a beam code written by M. Tournianski.

MSESIM calculates and returns all four stokes vector components as a function of wavelength. This stokes vector is then propagated through the Mueller matrix as outlined in Eq.3 to give S_{out}. The S0 component of S_{out} is the intensity on the CCD sensor, which can be digitised according to the specifications of the camera to provide realistic synthetic images.

3.2 Forward Modelled Images

Fig. 7 shows a forward modelled image as taken with the TSSSH IMSE system design. An image with the interference pattern is shown with the FLC with its axis orientated to 45°. The second shows the Fourier transform of the image, where the carrier frequency and DC frequency are present, with some broadband low level noise. The demodulation process consists of bandpass filtering around the carrier frequency to extract the phase information for each image. The difference in the phase of the two images recovers the 2D polarisation angle profile.
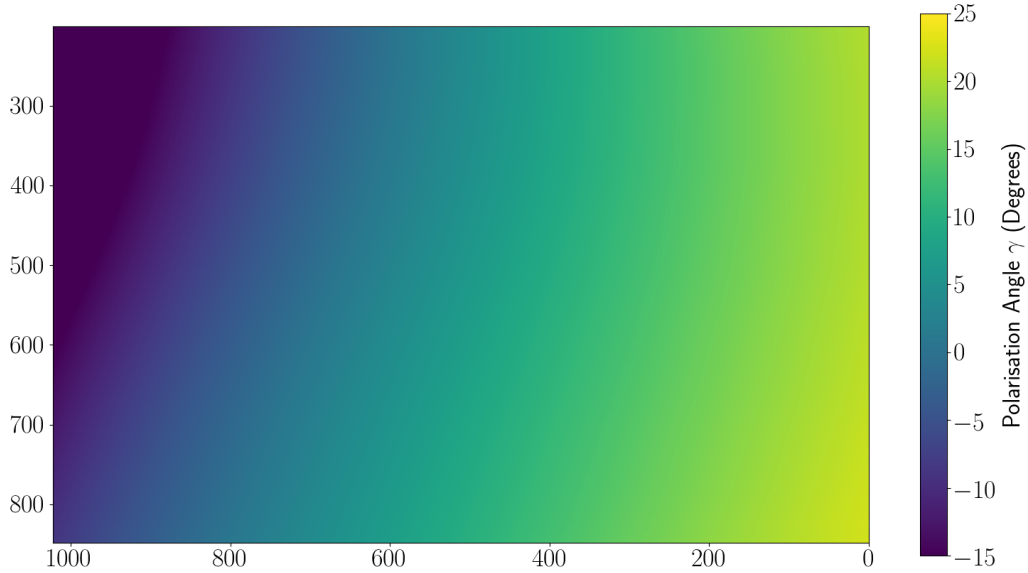

Figure 6: The ideal 2D polarisation angle γ recovered from demodulating the forward modelled images.
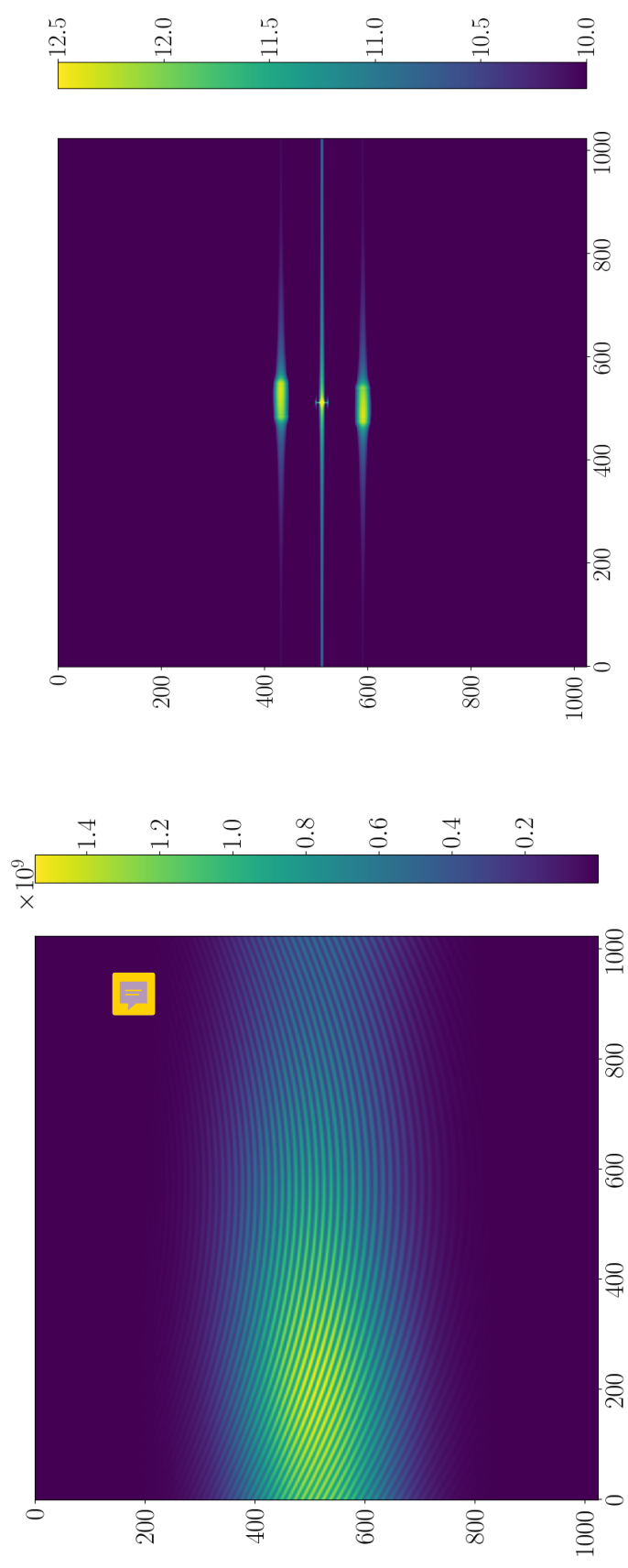
Figure 7: Left to Right: Forward modelled image produced by the TSSSH system, where the intensity is measured in photons per second. The FLC axis is orientated of 45°. The Fourier transform power spectrum of the image, with the carrier frequency and DC frequency shown. A forward modelled image is produced in each of the FLC states and are demodulated to retrieve the 2D polarisation angle profile in Fig6.
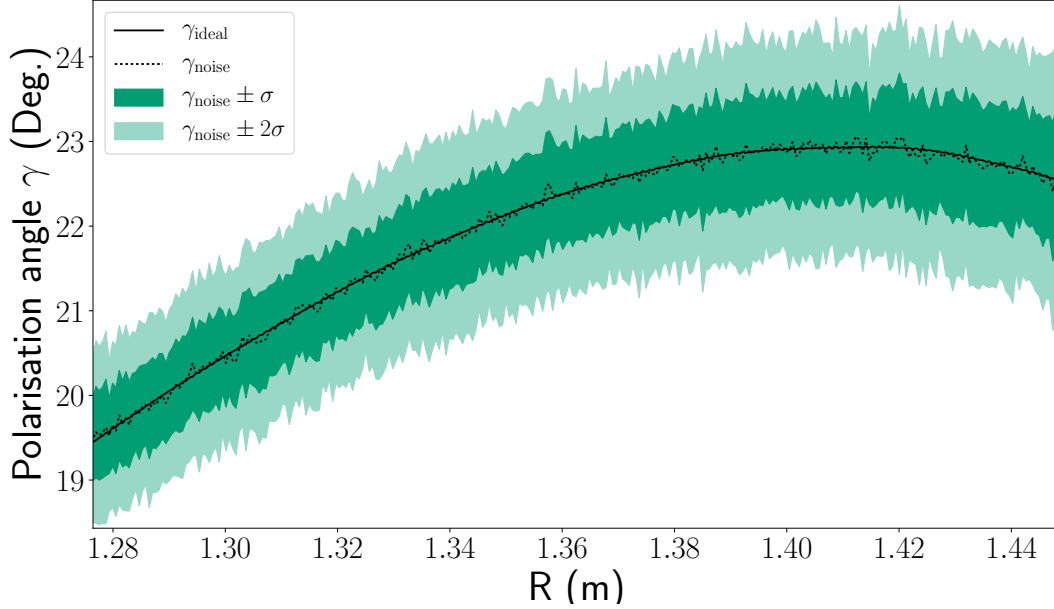
Figure 8: A 1D horizontal slice through the center of a noisy forward modelled image. Ideal polarisation angle profile γ_{ideal} is retrieved by demodulating using two images where non-ideal crystal effects and shot noise is neglected. 1σ and 2σ confidence intervals on the noisy polarisation angle profile are shown. This uncertainty could be reduced through longer exposure times or averaging over several frames.

An estimate of the standard deviation in the polarisation angle given the sensitivity of the camera was calculated. Photon shot noise was simulated by random sampling of a Poisson distribution with a mean given by the count rate $\lambda = I\tau$ where τ=1ms is the exposure time. To measure inter-ELM evolution of the current profile, an exposure time of τ=1ms is required. Dark noise and read noise were included by sampling Gaussian distributions centered around the measured values for the camera. The images were then digitized according the the sensitivity of the camera sensor. Both images were demodulated to retrieve the polarisation angle. The standard deviation shown in Fig.8 in the measurement was found to be σ=±0.5° at 1ms exposure time, which is equivalent the uncertainty in the conventional MSE measurements.

3.3 Forward Modelled Measurements with MAST-U Equilibrium

A FIESTA equilibrium was used to show the capabilities of the diagnostic within the scope of the MAST-U campaign. The equilibrium shown in Fig.9 is a MAST-U H mode plasma, with full NBI power of 7.5MW, an outboard radius of R=1.34m and inboard radius of R=0.355m, high elongation and low inductance. The same demodulation method was followed as outlined in section 3.2 to retrieve the polarisation angle γ profile. Fig.10 shows an increase in the polarisation angle at the plasma edge (R=1.31-1.34m). Fig.11 shows a zoom into the pedestal region where the flux contours Ψ=0.9 and Ψ=1 are overlaid. The realistic recoverable vertical extent is $\delta Z = 10$cm, which is approximately the height of the injected beam. Some ringing effects are present in Fig.11 at the edge of the image, caused by using a box filter in the demodulation process. Further work will be done to refine the demodulation process to improve the output profiles.

The vertical component of the magnetic field B_z can be recovered from the polarisation angle profile,

$$B_z = \frac{(A_5 \tan(\gamma) - A_2)B_\phi}{A_0 - A_3 \tan(\gamma)} \tag{7}$$

where A_0, A_3 and A_5 are geometric coefficients associated with the calibration and viewing geometry of the diagnostic, γ is the measured polarisation angle and B_ϕ is the toroidal magnetic field. Terms relating to
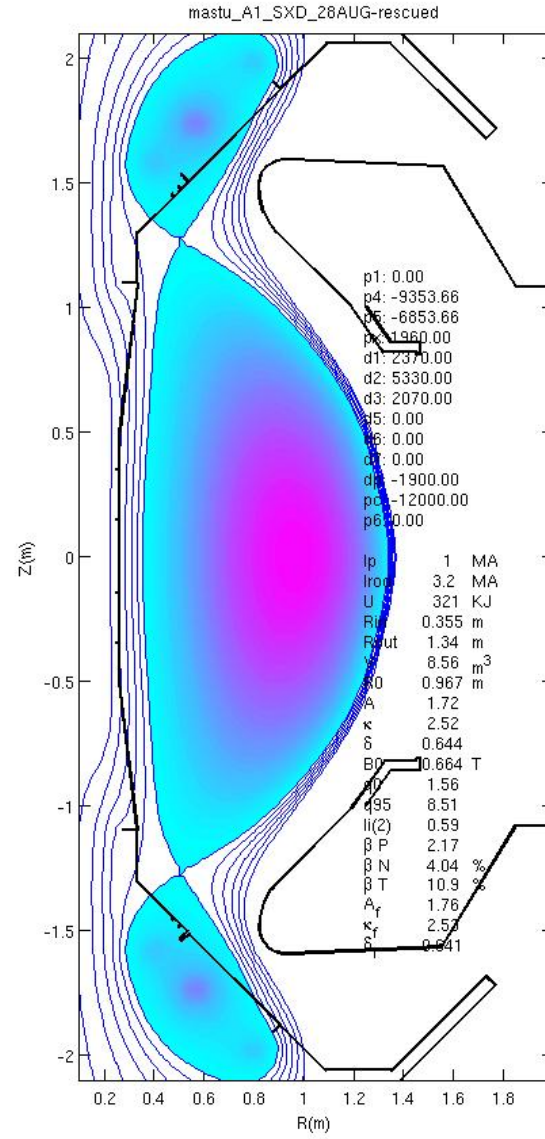
Figure 9: FIESTA generated MAST-U equilibrium used in the MSESIM forward model
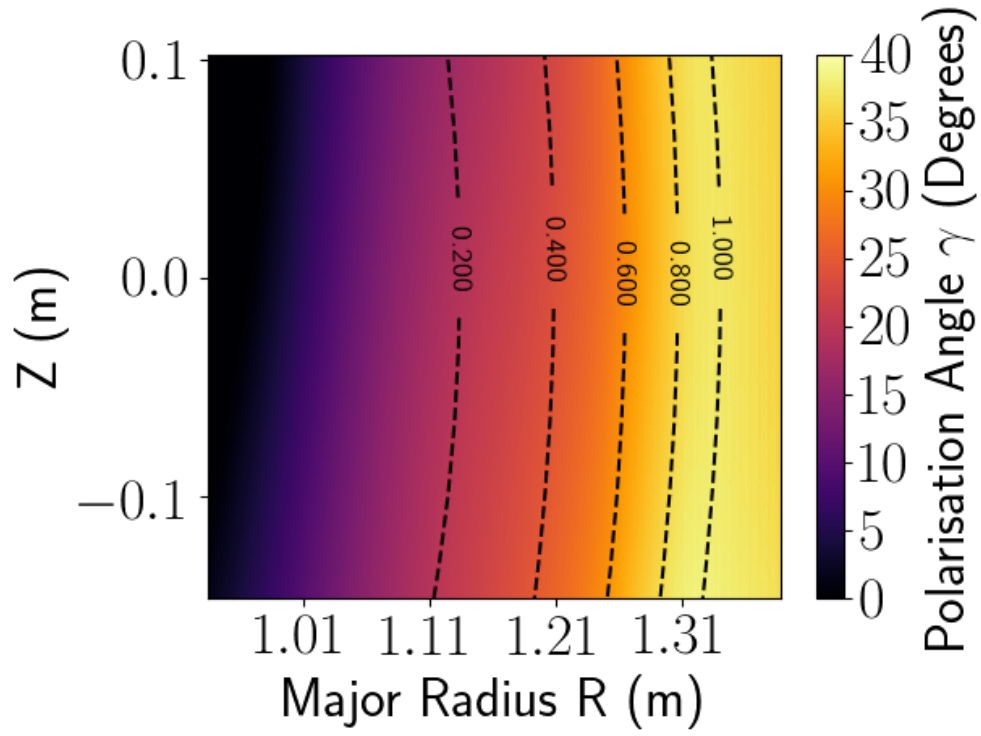
Figure 10: Polarisation angle profile across the full radial extent. Normalised flux contours are overlaid as black dashed line, to the plasma edge at $\Psi=1$.
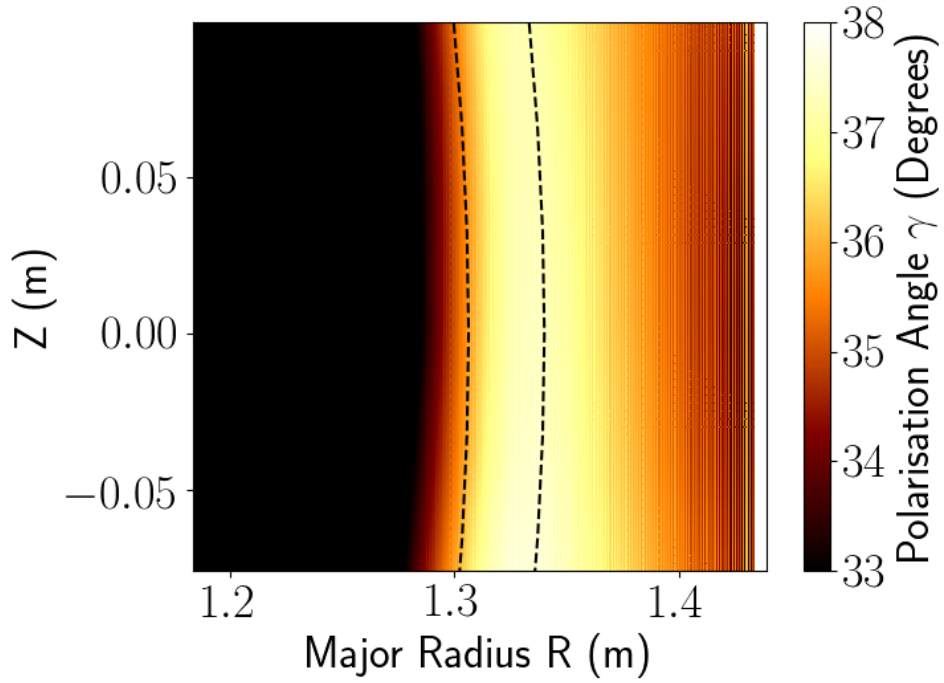

Figure 11: Polarisation angle profile at the plasma edge, with $\psi=0.9$ and $\psi=1$ contours. Some ringing artifacts are present at the very edge of the image which is caused by box filtering in the image demodulation process.
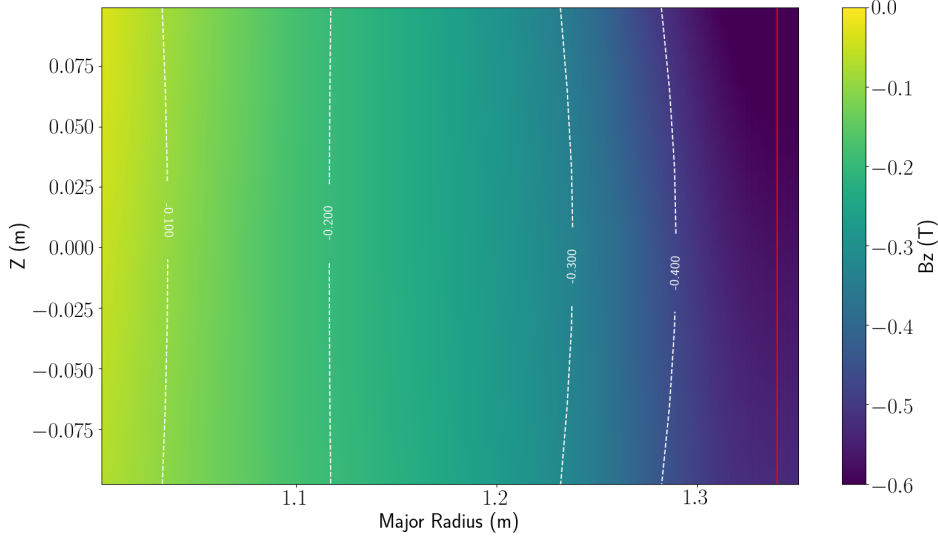
Figure 12: Recovered Bz profile from the demodulated polarisation angle profile. Bz contours from the initial equilibrium are overlaid in dashed white. The radial position of the separatrix is shown in red.

B_r have been assumed to be small, and taking B_ϕ from the FIESTA equilibrium along with the forward modelled 2D polarisation angle profile, the recovered B_z profile is shown in Fig.12, which matches to the contours (white dashed) input B_z profile.

3.4 Detector

The detector used is the Photron-SA4 fast camera, which is capable of providing exposure times down to the 1ms required for studying inter-ELM dynamics. The camera has previously been used in the coherence imaging spectroscopy system on MAST-U [11]. The limiting specifications of the camera include: Read out noise, which is high due to noise on the signal amplifier, the quantum efficiency is poor at 660nm (around 40%.) Baseline digitization conversion factor was measured to be 11.6±0.1 electrons/count [12], which also significantly lowers the signal to noise. The signal to noise was analytically calculated using the camera specifications and taking the number of photons incident on the detector n_γ in photons/s output from the forward model,

$$I = n_\gamma F \eta \tau G \tag{8}$$

where F is the fill factor of the pixels, η is the quantum efficiency of the detector and G is the detector gain. The signal to noise is,

$$\text{S/N} = \frac{I}{\sqrt{\sigma_{\text{read}}^2 + \sigma_{\text{shot}}^2 + \sigma_{\text{dark}}^2}} \tag{9}$$

One option to improve camera signal to noise would be to bin pixels in the vertical direction. This sacrifices resolution in z, but preserves the radial resolution. Another option is temporal averaging over successive frames or running at a slower exposure time (2-3ms).

3.5 Spatial Resolution

The radial resolution of the diagnostic is determined by several factors: The radial extent over which emission is observed for each line of sight, the width of the neutral beam and line of sight tangency to magnetic flux
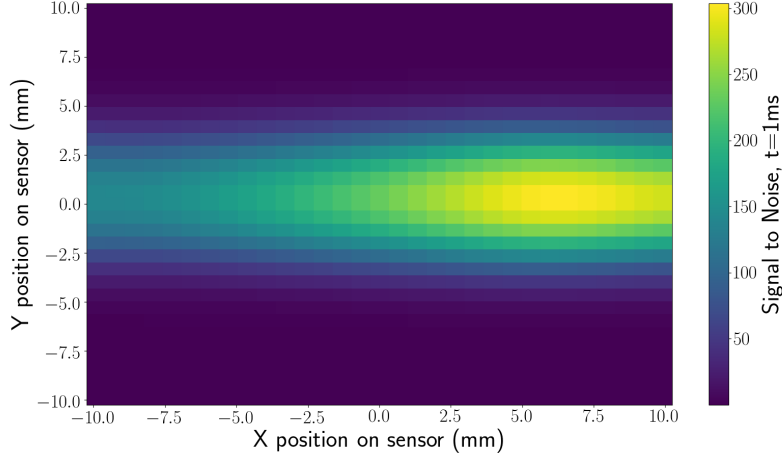
Figure 13: Signal to noise (S/N) ratio of the Photron-SA4 camera across the sensor, as a function of exposure time. S/N was calculated using the average photon count from MSESIM for the parameters described in Sec.3.1.

surfaces. The radial resolution was calculated by determining the major radii extent over which 80% of the emission intensity is captured, shown in Fig. 14. For edge measurements, the optical axis will need to be shifted horizontally 10cm in order to fully capture the plasma edge. It is not possible to improve upon the radial resolution of either the conventional or imaging MSE system unless a different port is used. The width of the beam and intersection angle between the beam and line of sight sets a fundamental limit on the maximum radial resolution that can be obtained. However, given the imaging system will provides more spatial information (in the form of more spatial measurements compared to the conventional system) it should be possible to see an improvement in the resolution of sharp edge features. The field of view of the diagnostic is shown in Fig.15 overlaid onto the equilibrium used in the MSESIM forward model. There is still good coverage of some of the plasma core, as well as the edge region of interest.

4 Implementation of the IMSE System

4.1 Port Allocation

The first measurements with the IMSE system will be for proof of diagnostic principle on low field, spherical tokamaks. The existing MSE port HM-07A is the ideal place to put the system, as the port is situated at the mid-plane, perpendicular to the SS neutral beam injector (NBI) and lines of sight are mostly tangent to flux surfaces. It would require removal of the conventional MSE system whilst IMSE measurements were taken, however it should be possible to find a couple of weeks within the MAST-U campaign to exchange the systems and take data. Once the IMSE system is attached to the port, it will not require any further manual intervention and can be operated through a triggering system. If these first measurements are of substantial benefit to the pedestal physics community, allocating a dedicated port for both the conventional system and IMSE system to run simultaneously would prove beneficial for diagnostic cross validation, with both edge and core measurements.

4.2 Data Acquisition and Storage Requirements

The IMSE system will run at the fastest temporal resolution of 1ms, operating at 1024x1024 pixels with a 12 bit ADC sensor. The size of each image then is,
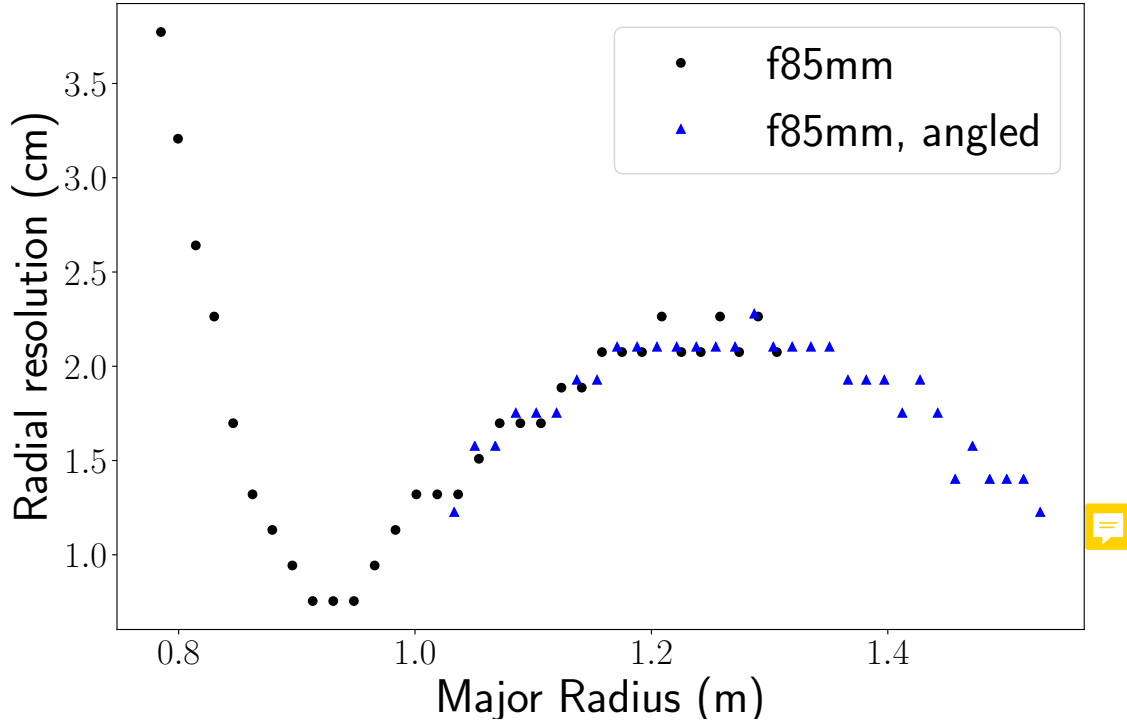
$$1024 \times 1024 \times 12 = 12.5 \text{Mb} \tag{10}$$

Figure 14: Radial resolution of each pixel using a collection optics lens with focal length f=85mm (black) and moving the optical axis of the diagnostic across by 10cm (blue). The optical axis can be shifted by angling the diagnostic on the port to give an improved field of view at the plasma edge.

Converting from bits to bytes, 1.57MB per frame. Running at 1ms, 1.57GB will need to be transferred every second from the camera. Total data taken in a 6 second MAST-U shot will be around 9.5GB, assuming the camera runs for the entire shot. The memory requirements for the demodulation process is, assuming 12 bit integer values are converted to 64 bit floats, 108MB per demodulation. To speed up any scheduler codes, it is faster to load the data into ECC memory of the data acquisition PC, rather than loading back from disk. Approx. 32GB of RAM should be plenty in order to both store the data in RAM, and perform the demodulation. The demodulation can then be parallelised with a multicore processor to provide fast post shot analysed IMSE data.

4.3   Calibration

Careful calibrations are required to understand any drifts that may occur in the polarisation angle measurement.

- An in-situ absolute calibration is desirable, where light of known polarisation is passed through the attached IMSE system to determine the absolute offset at each detector line of sight.

- Taking an image with the camera from the port can be used in CALCAM to provide a spatial calibration of the system.

- Non linearity of the optical components can cause polarisation angle offsets. These can be measured on the lab bench with an integrating sphere and rotating polariser, similar to how the conventional system is calibrated.
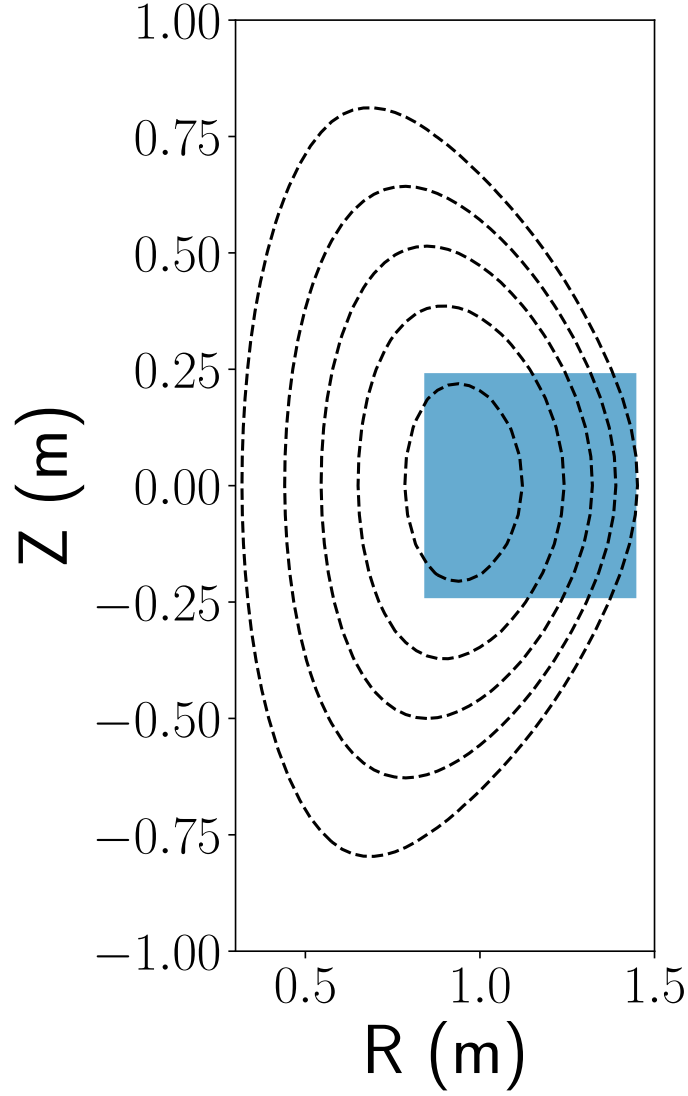
Figure 15: Field of view (FOV) of the diagnostic (light blue) from the current MSE mid-plane port. FOV is mapped onto normalised poloidal flux cross section. The contours are evenly spaced up to $\Psi_N=1$. The equilibrium is from a previous MAST shot (18501, t=0.29s)

- Faraday rotation calibration. After IMSE system is attached, shine polarised light into vessel, ramp individiual poloidal field coils and then the toroidal field to calculate the polarisation angle drift as a function of the toroidal and poloidal fields. This has not been done previously for the conventional system, but works well for Faraday rotation corrections to the IMSE data at AUG.

- Reverse Bt calibration. Forward and reverse toroidal field shots to find the crossing point of the polarisation angles for each radial channel, which gives a channel to channel offset.

5 Timeline, Work Requirements and Cost

The crystals have the longest lead time, quoted as 6-7 weeks from Bluebean optics. Other components such as the rotation mounts, can be bought with 2-3 days delivery time. Further time and costs will need to be allotted for the drawing office to design and manufacture small holders for the crystals within the Thorlabs mounts. A month has been allocated for bench calibrations to ensure the system works as expected and systematic offsets can be accounted for, which are caused by non-linear effects in the crystals. Several weeks will be needed to discuss and work with the data acquisition team to ensure data from the diagnostic is handled appropriately and saved to the central database.
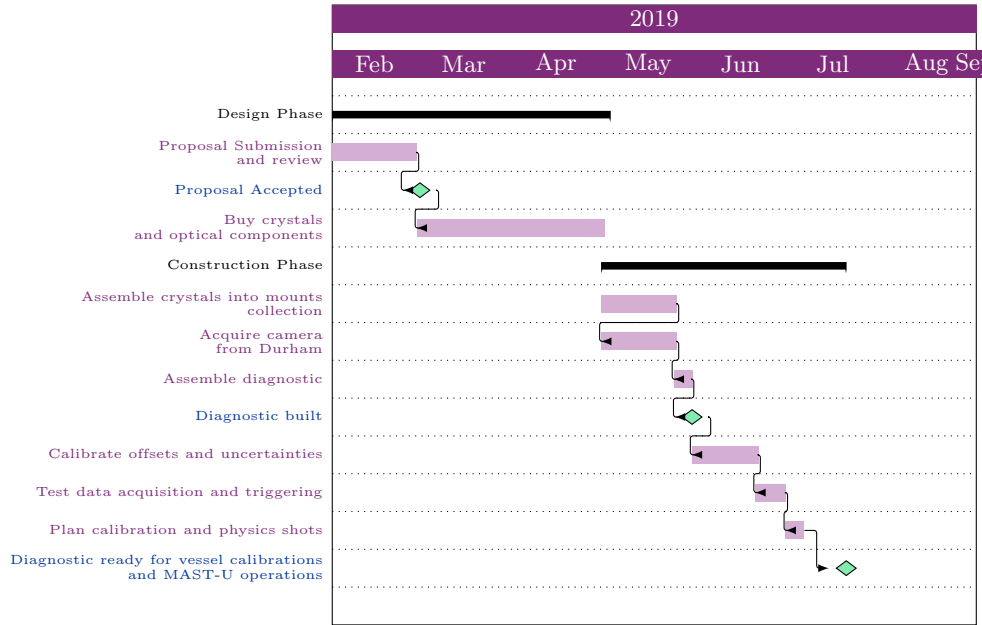

Figure 16: A breakdown of the necessary steps and milestones to achieve to have the IMSE system ready for MAST-U operations.

Further work requirements would be needed to work with a mechanical designer to design a suitable mount for the IMSE system. One solution would be to replicate the mount used in for coherence imaging system, which has a similar diagnostic setup to the IMSE system.

6 Future Upgrades

Possible future upgrades include moving the IMSE system to a dedicated port, ideally on the SS beam to provide cross validation of measurements with the conventional MSE system. A desirable hardware upgrade to the system would be a camera with improved gain and readout noise, such as the Photron SA-X2, to improve the signal to noise level. Implementing a full temperature control for the crystals would be desirable to stabilize against temperature induced birefringence in the crystals. With appropriate notice and calibrations, investing in a range of collection lenses and wider bandpass filters would allow full flexibility of the system such that the physics focus could be changed from edge to core between campaigns.

7 Acknowledgements

Item	Cost per item	Quantity	Cost
Optics			
Nikon f mount lens	£1,550	1	£1,550
Aspheric lens	£184.38	2	£368.76
Crystals			
Alpha-BBO delay plate	£2,430	1	£2,430
Alpha-BBO displacer plate	£2,103	1	£2,103
Alpha-BBO savart plate	£3,400	1	£3,400
Quarter wave plate	£200	1	£200
FLC Rotator	£4,000	1	£4,000
FLC Controller	£1,700	1	£1,700
Mounts			
Rotation mounts	£160	4	£640
Optical epoxy adhesive	£60	1	£60
Computing			
Acquisition PC with at least 32GB ECC RAM	£2,000	1	£2,000
Ethernet to fiber optic converter	£100	2	£200
Ethernet cable cat5	£30	1	£30
Miscellaneous			
Shipping costs	£200	1	£200
TOTAL			**£18,882**

Table 1: Breakdown of estimated costs for the IMSE system

8 Appendix A: Mueller matrices of optical components

The general Mueller matrix for a polariser with a polarisation angle θ,

$$P(\theta) = \frac{1}{2} \begin{pmatrix} 1 & \cos 2\theta & \sin 2\theta & 0 \\ \cos 2\theta & \cos^2 2\theta & \sin 2\theta \cos 2\theta & 0 \\ \sin 2\theta & \cos 2\theta \sin 2\theta & \sin^2 2\theta & 0 \\ 0 & 0 & 0 & 0 \end{pmatrix} \tag{11}$$

For a polariser at $\theta = 45°$,

$$P(\theta = 45°) = \frac{1}{2} \begin{pmatrix} 1 & 1 & 0 & 0 \\ 1 & 1 & 0 & 0 \\ 0 & 0 & 0 & 0 \\ 0 & 0 & 0 & 0 \end{pmatrix} \tag{12}$$

The Mueller matrix R(ρ) describes an arbitrary rotation around an axis angle ρ,

$$R(\rho) = \begin{pmatrix} 1 & 0 & 0 & 0 \\ 0 & \cos \rho & \sin \rho & 0 \\ 0 & -\sin \rho & \cos \rho & 0 \\ 0 & 0 & 0 & 1 \end{pmatrix} \tag{13}$$

The general Mueller matrix for a uni-axial waveplate which imparts some phase delay ϕ, orientated at an arbitrary angle ρ

$$W(\phi, \rho) = \begin{pmatrix} 1 & 0 & 0 & 0 \\ 0 & \cos^2 2\rho + \cos \phi \sin^2 2\rho & (1 - \cos \phi) \sin 2\rho \cos 2\rho & -\sin \phi \sin 2\rho \\ 0 & (1 - \cos \phi) \sin 2\rho \cos 2\rho & \sin^2 2\rho + \cos \phi \cos^2 2\rho & \sin \phi \cos 2\rho \\ 0 & \sin \phi \sin 2\rho & -\sin \phi \cos 2\rho & \cos \phi \end{pmatrix} \tag{14}$$

The Mueller matrix for a general waveplate at $\rho = 0°$ [?],

$$W(\phi, \rho = 0) = \begin{pmatrix} 1 & 0 & 0 & 0 \\ 0 & 1 & 0 & 0 \\ 0 & 0 & \cos \phi & \sin \phi \\ 0 & 0 & -\sin \phi & \cos \phi \end{pmatrix} \tag{15}$$

The Mueller matrix for a savart plate W(ϕ_s), two uni axial waveplates with $\theta = 45°$, $\rho = 45°$ for the first plate and $\rho = 135°$ for the second plate,

$$W(\phi_s) = R(-\rho_1) \cdot W(\phi_{s1}) \cdot R(\rho_1) \cdot R(-\rho_2) \cdot W(\phi_{s2}) \cdot R(\rho_2) \tag{16}$$

References

[1] F. M. Levington, R. J.Fonck, G. M. Gammel, R. Kaita, H. W. Kugel, E. T. Powell, and D. W. Roberts, Phys. Rev. Lett. **63**(19), (1989)

[2] J. Howard, Plasma Phys. Control. Fusion, **50**(12), (2008)

[3] N. J. Conway, M. F. M. De Bock, C. A. Michael, M. J. Walsh, P. G. Carolan, N. C. Hawkes, E. Rachlew, J. F. G. McCone, S. Shibaev, and G. Wearing, Rev. Sci. Instrum, **81**(10), (2010)

[4] M. F. M. De Bock, J. Citrin, S. Saarelma, D. Temple, N. J. Conway, A. Kirk, H. Meyer, C. A. Michael and the MAST team, Plasma Phys. Control. Fusion, **54**(2), (2012)

[5] O. P. Ford, A. Burckhart, R. McDermott, T. Pütterich, R. C. Wolf, and ASDEX Upgrade Team, Rev. Sci. Instrum. **87**(11), (2016)

[6] J. Howard, C. Michael, H. Chen, R. Lester, A. Thorman, J. Chung, J. Instrum, **10**(9), (2015)

[7] J. Wesson and D J. Campbell, Tokamaks, Vol. 149, Oxford University Press, (2011)

[8] P. J. McCarthy, P. Martin, and W. Schneider, IPP Report, (1999)

[9] A. Burckhart, O. P. Ford, A. Bock, R. Fischer, M. Reich, D. Rittich and the ASDEX Upgrade team, 45th EPS Conference on Plasma Physics, (2018)

[10] M. F. M. De Bock, N. J. Conway, M. J. Walsh, P. G. Carolan, and N. C. Hawkes, Rev. Sci. Instrum **79**10 (2008)

[11] S. Silburn, Durham University Thesis, (2014)

[12] J. Allcock, private communication (2018)